Split-Flaps – a Way to Improve the Heel Stability of T-Foil Supported Craft

(article starts on next page)

Split-Flaps – a Way to Improve the Heel Stability of T-Foil Supported Craft

N.S.S. Prabahar
Ph.D. Student, Department of Marine Sciences, University of Gothenburg, Gothenburg, Sweden.
nimal.sudhan.saravana.prabahar@gu.se

A. Persson
Ph.D. Student, Chalmers University of Technology, Gothenburg, Sweden & Project Manager,
SSPA Sweden, Gothenburg, Sweden

L. Larsson
Professor Emeritus, Department of Mechanics and Maritime Sciences, Chalmers University of
Technology, Gothenburg, Sweden

Abstract. Horizontal T-foils allow for maximum lift generation within a given span. However, the lift force on a T-foil acts on the symmetry plane of the hull, thereby producing no righting moment. It results in a lack of transverse stability during foil-borne sailing. In this paper, we propose a system, where the height-regulating flap on the trailing edge of the foil is split into a port and a starboard part, whose deflection angles are adjusted to shift the centre of effort of the lift force. Similar to the ailerons which help in steering aircraft, the split-flaps produce an additional righting moment for stabilizing the boat. The improved stability comes, however, at a cost of additional induced resistance.

To investigate the performance of the split-flap system a new Dynamic Velocity Prediction Program (DVPP) is developed. Since it is very important for the performance evaluation of the proposed system it is described in some detail in the paper. A complicated effect to model in the DVPP is the flow in the slot between the two flaps and the induced resistance due to the generated vorticity. Therefore, a detailed CFD investigation is carried out to validate a model for the resistance due to the slot effect.

Two applications of the split-flap system: an Automated Heel Stability System (AHSS) and a manual offset system for performance increase are studied using a DVPP for a custom-made double-handed skiff. It is shown that the AHSS system can assist the sailors while stabilizing the boat during unsteady wind conditions.

The manual offset enables the sailors to adjust the difference between the deflection angles of the two flaps while sailing, thus creating a righting moment whenever required. Such a system would be an advantage whilst sailing with a windward heel. Due to the additional righting moment from the manual offset system, the sails could be less depowered by the sailors resulting in a faster boat despite the additional induced resistance.

It is shown in the paper that the control systems for the ride height and the heel stability need to be decoupled. The paper ends with a description of a mechanical system that satisfies this requirement.

Keywords: Hydrofoil; Split-Flaps; Transverse Stability; DVPP.

NOMENCLATURE

AR_e	Effective Aspect Ratio [-]
b	Beam [m]
$C_{D,i}$	Induced drag coefficient [-]
C_L	Lift coefficient [-]
$C_{L,2D}$	2-Dimensional lift Coefficient [-]
$C_{L,3D}$	3-Dimensional lift Coefficient [-]
F	Force Residuals [N]
f	Flap angle [deg]
f_o	Optimal flap angle [deg]
f_p	Portside flap angle [deg]
f_s	Starboard flap angle [deg]
h	Ride height [m]
I	Mass Moment of Inertia of the Boat [kg m^2]
K_c	Response coefficients of the sailor control system [-]
M	Moment Residuals [N m]
m	Mass of the boat [kg]
p	Roll rate [rad s^{-1}]
u	Linear boat velocity in x-direction [m s^{-1}]
v	Linear boat velocity [m s^{-1}]
$\dot{v}$	Linear acceleration [m s^{-2}]
w	Linear boat velocity in z-direction [m s^{-1}]
α_i	Angle of attack [deg]
φ	Heel angle [deg]
$\dot{\varphi}$	Heel rate [deg s^{-1}]
θ	Pitch angle [deg]
$\dot{\theta}$	Pitch rate [deg s^{-1}]
ψ	Yaw angle [deg]
$\dot{\psi}$	Yaw rate [deg s^{-1}]
ρ	Density of water [kg m^{-3}]
ω	Angular roll velocity [rad s^{-1}]
$\dot{\omega}$	Angular acceleration [rad s^{-2}]
AHSS	Automated Heel Stability System
AR	Aspect Ratio
CAD	Computer-Aided Design
CE	Centre of Effort
CFD	Computational Fluid Dynamics
CG	Centre of Gravity
DOF	Degree of Freedom
DVPP	Dynamic VPP
EOM	Equations of Motion
GC	Gain Coefficient
RANS	Reynolds Averaged Navier-Stokes
RM	Righting Moment [Nm]
TCG	Transverse Centre of Gravity of the sailors
TE	Trailing Edge
TWA	True Wind Angle [deg]
TWS	True Wind Speed [m s^{-1}]
VPP	Velocity Prediction Program

1. INTRODUCTION

One of the most common foil configurations for lighter dinghies is the T-foil. It is favoured for foiling dinghies with high lift requirements and has better structural characteristics compared to cantilever foils (Monsonnec and Waller, 2015). T-foil configurations usually consist of a single main horizontal foil and a vertical centreboard connecting the horizontal foil to the hull such that the lift of the foil acts in the centreplane of the boat. Such configurations also have a smaller horizontal foil attached to the rudder board to stabilize the boat in pitch (Beaver and Zseleczky, 2009).

For larger foiling craft (AC50 and AC75 etc.), the layout contains separate leeward and windward foils, where only the leeward foil is in the water, thereby generating a large righting moment. See Larsson *et al* (2022). With a single T-foil foiling craft suffer from a lack of transverse stability. Thus, the stability of the boat is crucially dependent on the sailor's position, which complicates the handling, particularly for double-handed skiffs. With righting moment from the hull lost while foiling, there is little room for error whilst handling the boat. During wind disturbances and manoeuvring, the control of the boat could become overwhelming for the average sailor.

To ease the sailor's efforts in balancing the boat, a system to produce an additional righting moment from the foils is studied in this paper. The Trailing Edge (TE) flap, used for T-foils to control the foiling height of the boat, is split in the centreplane into a starboard and port flap. Deflecting the split-flaps at different angles will shift the Centre of Effort (CE) producing a righting moment
However, the righting moment comes at a cost. There is a very complex flow between the split-flaps, generating a trailing vortex, and the strength of the tip vortices may also be increased. So, there will be an increase in induced resistance.

An explanation of the proposed system and its effect is presented in Section 2, followed, in Section 3, by a description of the test case, the double-handed skiff *Linnea,* designed for the very light winds off Palermo in late September. In Section 4 a newly developed Dynamic Velocity Prediction Program (DVPP) is introduced. Since this is very important for the evaluation of the performance of the proposed system it is presented in some detail. In order to model the effect of the complicated flow between the two flaps a systematic CFD investigation was carried out. It is presented in Section 5 and the result is used in the DVPP. Results from DVPP computations are reported in Section 6, where the performance of the proposed system is analysed in detail. It is shown that for maximum performance the ride height and heel stability control systems have to be independent, and a mechanical system with this capability is introduced in Section 7. Finally, several conclusions are presented.

2. SPLIT TRAILING EDGE FLAPS ON T-FOIL CONFIGURATIONS

Split trailing-edge flaps operate similar to aircraft ailerons: by deflecting the flap down, for instance on the starboard side, and up on the port side, the lift force is increased on the starboard side and reduced on the port side. The difference in lift force shifts the CE to starboard and the corresponding moment tends to rotate the boat towards the port side. Figure 1 shows the split flaps on a horizontal foil with the port flap (blue) deflected upwards and the starboard flap (red) deflected down.
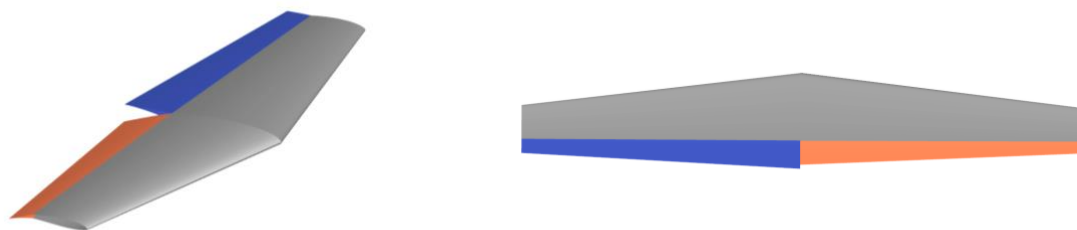

Figure 1. Split flaps on a horizontal foil – Port flap (blue) and starboard flap (red)

2.1 Forces on T-Foil Configurations

In figure 2, the major force components contributing to the transverse stability of a heeled foiling sailboat are presented. The heeling moment towards the leeward side is produced by the sail force and the appendage side force, and the righting moment towards the windward side is produced by the gravity force of the boat and sailors. The lift force acts through the Centre of Gravity (CG) of the hull and does not produce a moment around the CG. With the gravity forces resolved into orthogonal components along the boat fixed coordinate system it can be observed that the horizontal component produces a heeling moment when the boat is heeled to leeward (Figure 2a). As seen in figure 2b, the horizontal component of gravity forces produces a righting moment (i.e. opposite to the heeling moment from the sails) with a windward heel. Thus, most sailors prefer to heel windward when foiling to increase the righting moment from the gravity force.
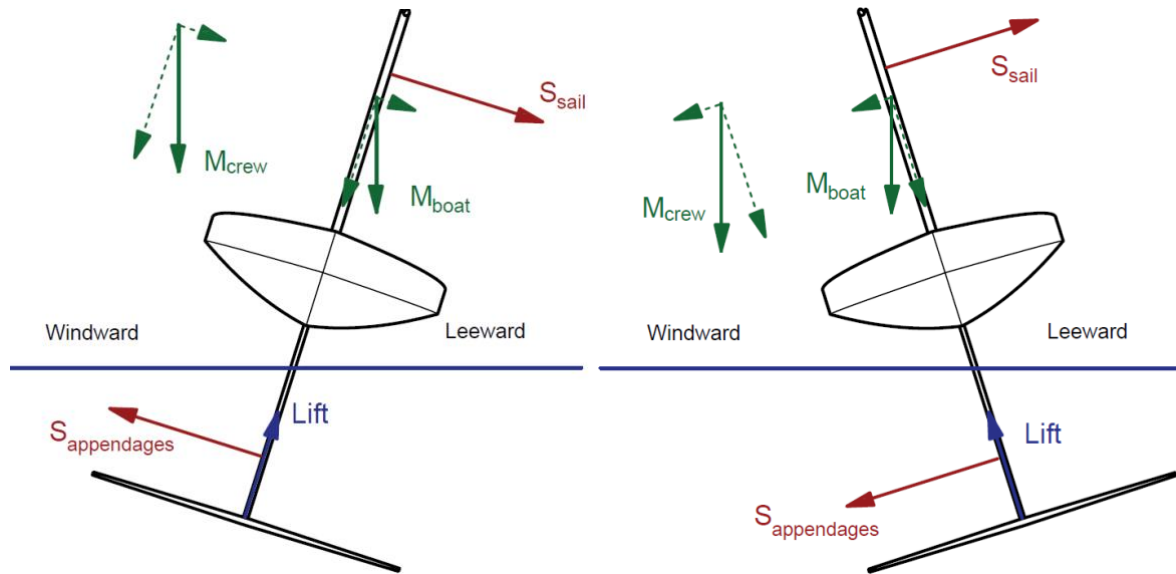

Figure 2. Transverse forces on a heeled sailboat – (a) Heeled to leeward (b) Heeled to windward

2.2 Foiling with the Automated Heel Stability System

The split-flaps are used with two applications: to increase stability during disturbances with the AHSS and to increase performance with the manual offset system. With the Automated Heel Stability System (AHSS), the split-flaps are deflected according to the heel angle of the boat, thereby an automated stabilizing response to the heel is generated. Figure 3 shows the forces acting on the boat while sailing with the AHSS. The lift force is shifted leeward while heeling leeward and produces a moment towards the windward side, and the opposite happens with a windward heel. AHSS would require an effective control system to measure the height and heel angle and adjust the individual flaps proportionately. The effectiveness during wind disturbances is studied using a DVPP.
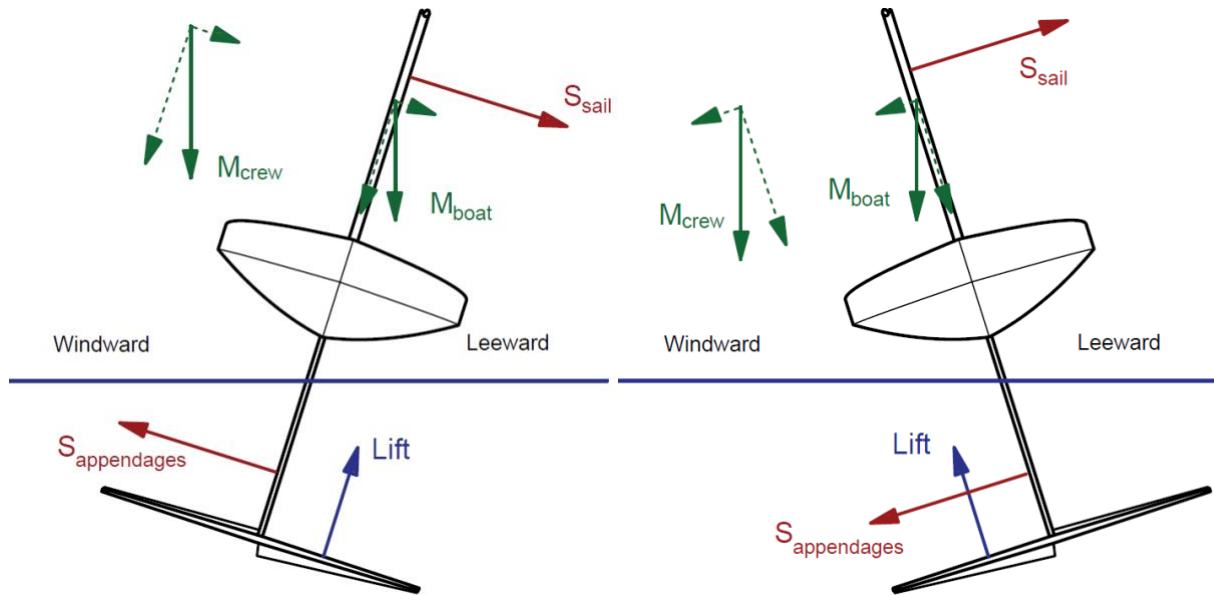
Figure 3. Forces on a heeled sailboat with AHSS – (a) Heeled to leeward (b) Heeled to windward

2.3 Foiling with the Manual Offset System

Since heeling windward increases the arm of the gravity forces, most sailors would prefer heeling to windward. As AHSS would oppose heeling windward, so, complimenting the AHSS, a mechanism that would let the sailors manually adjust the difference between the deflection angles of the split-flaps is added. The offset refers to shifting the ideal heel angle the AHSS should maintain. Without the offset, the AHSS would try to maintain a zero heel angle and using the offset the AHSS could be forced to maintain a windward heel. The 'manual offset' will be useful to shift the CE of lift towards leeward while heeling windward (Figure 4). Thereby, maximizing the righting moment from the gravity forces and yet producing an additional righting moment from the foils. Due to the additional stability, the sailors could increase the power on the sails and increase the boat speed.
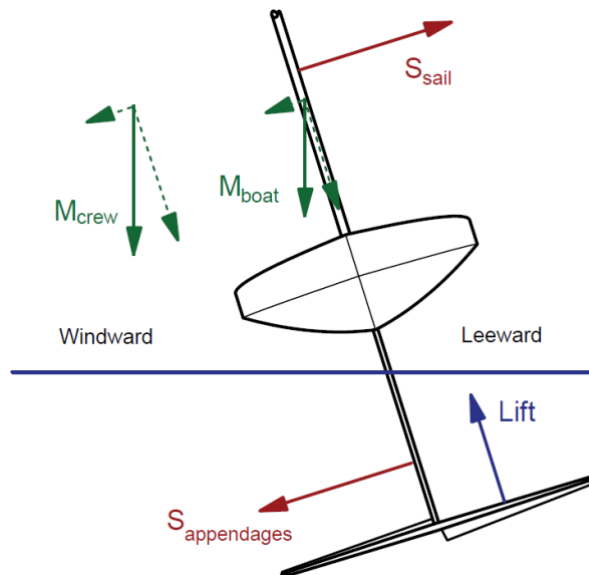

Figure 4. Sailing with the manual offset with a windward heel

5

3. TEST CASE

The test case for this study is a 4.6 m long skiff designed and built by the students from the Naval Architecture and Ocean Engineering Master's program at Chalmers University of Technology to compete for the *1001Vela Cup* in 2018. This double-handed skiff "*Linnea*" has a displacement of 149 kg excluding the sailors when fully rigged. The design of Linnea was inspired by the Olympic 49er class but adapted to the low wind speeds expected at the race venue, with a taller mast and larger upwind sail plan (Acerbi et al, 2017). These large sails and rigging, in turn, shift the CG upwards making the boat highly unstable, even without foils. The original design was a non-foiling skiff, but recent changes in regulations to allow high-performance materials support the idea of foiling. The project for the year 2020 was to design foils for the existing hull and T-foil configurations were considered to maximize the lift generated. Being an unstable double-handed skiff, *Linnea* is very difficult to balance even without foils, and in foil-borne conditions, it would hardly be possible using a standard T-foil configuration. The 2020 regatta was conducted as a design competition due to the COVID-19 pandemic and hence the foils designed for Linnea has not been manufactured.

3.1 Foil Design

The skiff is designed in compliance with the R3 class rules of 1001Vela Cup[1], which for instance states that the overall breadth including appendages is limited to 2.1 m. Since the wind speed is very low, any foil configuration should make use of the entire span to generate a reasonable lift. Configurations with separate port and starboard foils would half the lift generated if only one side is lowered and would be hard to handle with just a crew of two.

Figure 5. The test case - *Linnea*

---

[1] The rules are available on url: 1001VEhttps://www.1001velacup.eu/regolamento.html. The class rules have been modified now to remove the span restriction, however, this happened quite late in the project when the design was already finalized

A horizontal foil layout was chosen to utilize the full 2.1 m span for lift generation. The foil will be submerged at all times, supported by the hull via the centreboard. The airfoil section is chosen as Wortmann FX-60100 (figure 6) due to the high lift to drag ratio at the low Reynolds numbers (Andersson et al, 2018). With the span limited, and the Taper Ratio set at 0.45 for minimum induced drag, only the chord length of the foil was free for optimization. A systematic parametric study was performed using a static Velocity Prediction Program (VPP) to estimate the mean chord length which will result in the lowest possible take-off True Wind Speed (TWS). Based on this study, a mean chord of 0.263 m was selected.
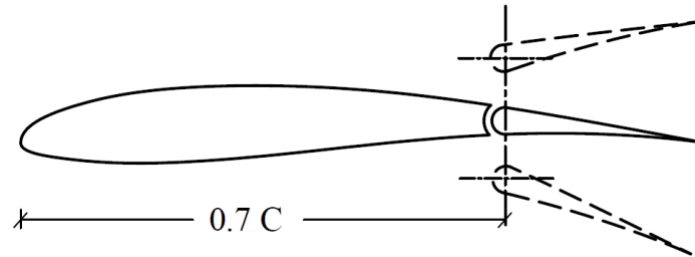

Figure 6. Cross-section of FX60100 showing the trailing edge flaps

3.2 Control System Design

For height regulation, the TE flaps were designed to be at 30 % of the local chord length to ensure optimal control over the lift (figure 6). The flap would ideally deflect between +12 degrees and -7 degrees (positive downward), set based on the reasoning that a flap deflection of -6.8 degrees corresponds to zero lift generation for this airfoil and flap length, and any flap angle greater than +10 degrees will increase the risk of flow separation.

3.2.1 Ride Height Control

Ride height is defined as the displacement of the boat in the vertical direction. To maintain a stable ride height and to prevent the boat from flying out of water, the TE flap angles need to be reduced (deflected upward) with an increase in ride height. There have been both electronic and mechanical control systems used to adjust the flaps. However, due to R3 class compliance, which prohibits the use of stored power, the system was designed to be purely mechanical. One of the most common ways is to use a surface skimming wand that follows the water surface. The wand is connected to the flaps using mechanical links. Since the wand skims the surface, when the boat rises, the wand is lowered, which in turn reduces the flap angle and consequently the lift force. The opposite happens when the boat falls. This system has been successfully applied in foiling moths for a long time, Beaver and Zseleczky (2009).

3.2.2 Control System for the Split-Flaps

For automated heel stability, two wands are used, on the maximum beam positions on the starboard and port side. Each wand would be connected only to the respective side of the split TE flap, such that each wand behaves as an individual ride height response system. When there is no heel, both wands are displaced in sync to adjust both flaps in proportion only to the ride height. As the boat heels, one wand is displaced upwards and the other downwards, and this deflects the respective flaps downward and upwards (figure 7). Using a cam fixed on the rotational axis of the wand, the rotation of the wand is transferred to the flaps using a push rod that follows the cam (See Boman, 2020). The two-wand system implicitly responds to heel as the change in the height on the respective side.
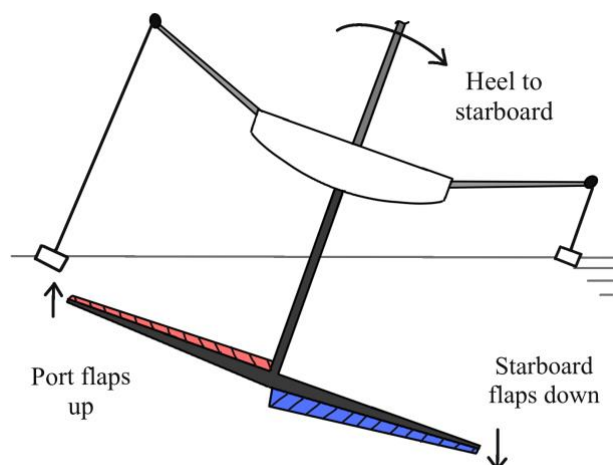
7

Figure 7. AHSS control system with two wands

An offset screw could be used in the mechanical links between the wand and the flaps to manually create a difference in the flap angles. This mechanism would be controlled by the sailors during the race to increase the righting moment and to heel windward with the AHSS. The design of such a system has been proposed by Boman (2020).

4. THE NEWLY DEVELOPED DVPP

4.1 DVPPs versus linearized approaches.

It is possible to check the flight stability of the boat in different modes through stability derivatives without fully solving the non-linear Equations of Motion (EOM). The EOM are linearized around an equilibrium point and motions are treated as small disturbances (Masuyama, 1987). The stability derivatives in each DOF are calculated and the eigenvalues of the resulting stability matrix provide details on the dynamic stability of the system in different modes. Masuyama (1987) provided a detailed study on the methods to compute the stability derivatives for a foiling sailboat and has stated the differences between the stability derivative approach and solving the non-linear EOM. During calculations of the stability derivatives, several assumptions were made to reduce the order of the equations, thereby reducing the accuracy of the method. Hence, Bagué et al (2021) used CFD to compute the stability derivatives for a foiling catamaran rather than the semi-empirical methods used by Masuyama. Though the stability derivatives provide data regarding the stability of the boat, dynamic simulations like disturbances and manoeuvring could not be studied.

A much more solid approach than using stability derivatives is to use a DVPP, which solves the EOM at each time step. 6 DOF dynamic simulations of aircraft have been studied extensively (Caughy, 2011) and it lays the foundation for the DVPP design for foiling sailboats. However, the dynamics of the sailboats are much more complicated than for an aircraft, due to the asymmetry of the boat and the variable CG of the system caused by the movement of the sailors. See Heppel (2015) for a comparison of the differences between aircraft and sailboat dynamics. Several DVPPs have been developed to analyse foiling sailing yachts in a numerical environment and optimize foil arrangements and sailing strategies. Hansen et al (2019) developed and used a DVPP with *FS-equilibrium* to optimize manoeuvres for the America's cup AC50 class. Eggert et al (2020) applied the *FS-equilibrium* DVPP to the foiling international Moth class.

In this paper, a new DVPP is developed to study the effectiveness of the split-flaps. The DVPP is a further development of a static VPP developed by Andersson et al (2018) in connection with the design of the foiling Optimist. During the design of foils for the test case, a static VPP was used for

estimating the optimal foil dimensions for foiling at the lowest True Wind Speed. The static VPP uses the same force models as the DVPP disregarding the dynamic effects. However, instead of solving for accelerations in each DOF, the state variables (speed, height, leeway etc.) are iterated until equilibrium is achieved in all DOFs.

4.2 Dynamics

Newton's second law of motion, which equates force as the mass times acceleration is the base equation used in the DVPP. It is only valid in an inertial frame of reference (non-accelerating and non-rotating) which is not the case for the sailboat. An inertial frame of reference would be a coordinate system fixed on earth (**O** in figure 8), however, calculating the forces and moments on the boat in earth fixed coordinates will be too complicated. Hence, all forces, moments, and motions are estimated through the centre of gravity of the body. The equations of motion through CG are given by equations 1 and 2.

$$F = m^*(\dot{v} + \omega \times v) \tag{1}$$

$$M = I^*\dot{\omega} + \omega \times I^*\omega \tag{2}$$

Where, $m^* = m + A$, and m is the total mass of the boat, and A is the added mass matrix in the respective DOFs. $I^* = I + IA$, and I is the mass moment of inertia along the axis of rotations and IA is the added inertia. F and M are the net force and moment residuals respectively, v and ω are the linear and angular velocities, with their respective accelerations $\dot{v}$ and $\dot{\omega}$.

For aircraft, the CG is almost always fixed in the body of the aircraft, and equations 1 and 2 could be applied without any changes. In the case of sailboats, the CG is varying due to the motion of the sailors, and computing the motions through a variable point in the body is resource-consuming. The net centre of gravity of the boat and sailors is shown as point **A** in figure 8. Point **G** is fixed on the boat at the centre of gravity of the rigged hull without the sailors. Fixing the body coordinates in point **G** would be convenient to calculate the force and moment residuals. Horel (2019) assumed the distance between the net CG and **G** to be zero and modelled the effect of the sailors as an external force. This assumption could hold well for large craft with the mass of the boat several times the mass of the sailors.

For smaller craft, such as *Linnea,* the boat mass is similar to the sailor's mass and the effect of the variable CG will be significant. Hence the assumption made by Horel (2019) would be too approximate for this case. The effect of the variable CG has been taken into account by Kerdraon et al (2020), such that the distance between **G** and **A** is non-zero. Equations 1 and 2 are modified to account for this. Bacon and Gregory (2007) derived the equations for a damaged asymmetric aircraft through an arbitrary point different from the CG of the aircraft (equations 3 and 4). As individual components, equations 3 and 4 are available in Kerdraon et al (2020)

$$F = m^*(\dot{v} + \omega \times v) + \dot{\omega} \times m^* R + \omega \times (\omega \times m^* R) \tag{3}$$

$$M = I^*\dot{\omega} + \omega \times I^*\omega + m^* R \times \dot{v} + m^*\omega \times (R \times v) + m^*v \times (\omega \times R) \tag{4}$$

Where R is the distance between **G** and **A**. Forces and moments are calculated through the body-fixed coordinate system at **G**.

Solving equations 3 and 4 gives the linear and angular velocities of the boat in the body-fixed coordinates. The orientation of the boat with respect to the earth fixed coordinate system is estimated by rotating the angular accelerations with the rotation matrices in equation 5.

$$\begin{bmatrix} 1 & \sin\varphi\tan\theta & \cos\varphi\tan\theta \\ 0 & \cos\varphi & -sin\varphi \\ 0 & \dfrac{\sin\varphi}{\cos\theta} & \dfrac{\cos\varphi}{\cos\theta} \end{bmatrix} \omega = \begin{bmatrix} \dot{\varphi} \\ \dot{\theta} \\ \dot{\psi} \end{bmatrix} \tag{5}$$
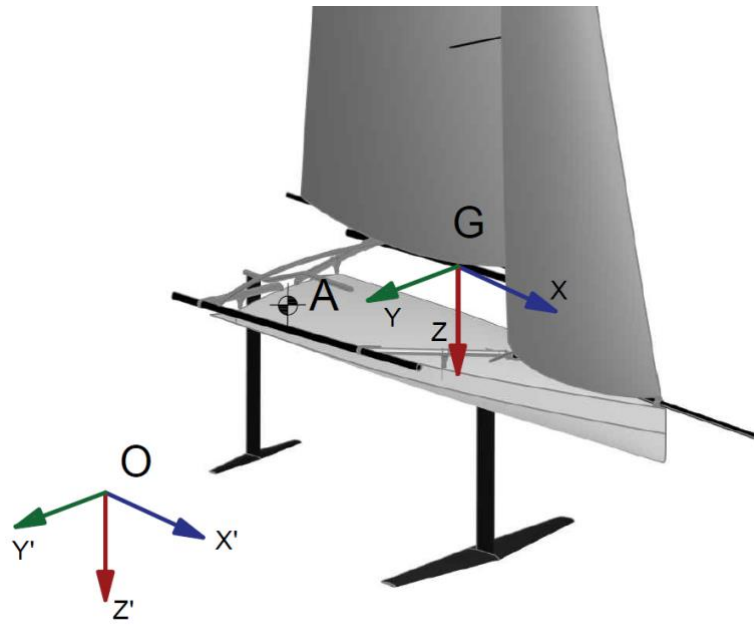
Figure 8. The coordinate system of the boat

Here the Euler angles φ, θ, and ψ are the roll, pitch, and yaw angles of the boat with respect to the earth fixed coordinates. Equations 3, 4, and 5 are solved using the *ode45* function in MATLAB (2020), which is an ordinary differential equation solver. The inputs to the solver are the rates of velocities in each DOF and the outputs are the velocities in the respective DOFs. It is not straightforward to estimate the rates of the velocities from equations 3 and 4 due to the non-linear coupling of the rotational accelerations in the linear acceleration equations and vice versa. Shampine et al (2003) suggest rearranging equations 3 and 4 as,

$$B * D = C \tag{6}$$

D is a column matrix containing the six derivatives of the velocities, namely $\dot{v}$ and $\dot{\omega}$. B is termed as a mass matrix and C is the remaining terms of equations 3 and 4. If B is a non-singular matrix, equation 6 can be solved as,

$$D = B^{-1} * C \tag{7}$$

The derivatives in matrix D can now be solved using MATLAB *ode45*.

4.2.1 Added Mass

While accelerating a body through a fluid, the surrounding fluid would also be accelerated contributing to the mass of the body as an added virtual mass, and the corresponding inertia is termed as added inertia. The added mass and added inertia for the hull are neglected as the added mass for the foils and appendages is significantly larger (Faltinsen, 2005). Added mass and inertias for unit chord length for the appendages are calculated using a strip-theory approximation for a flat plate (equation 8), Eggert et al (2020).

$$m_{22} = \pi \rho t^2 \qquad m_{66} = \frac{1}{8\pi\rho t^4} \tag{8}$$

where $2t$ is the strip width of the appendage, $m22$ and $m66$ are the added mass in vertical and rotational accelerations, respectively. The same approach is followed for calculating the added mass of the sails

4.2.2 Damping

Damping due to the foils and appendages is modelled as the quasi-static change in the angle of attack (α_i) of the flow to the appendages and sails (equation 9). When the boat moves upwards, the foil experiences a downward flow, thereby reducing the angle of attack and the lift produced (Eggert et al 2020). The opposite happens when the boat moves down. For roll-damping, when the boat rolls to port, the port side moves down and faces an upward flow, increasing the angle of attack and the lift force on the port side. The appendages are split into chord-wise strips and the instantaneous flow angle and velocity at the strips are estimated. Using the instantaneous α_i, the forces on each strip are calculated, which are added to other strips span-wise to obtain the total forces on the appendages.

$$\alpha_i = tan^{-1}\left(\frac{w}{u}\right) \tag{9}$$

w is the vertical velocity and u is the horizontal velocity. Damping due to the sails is also accounted as the change in the instantaneous angle of attack of sails due to the boat motions.

4.3 Force Models

Forces in the DVPP are computed with a combination of semi-empirical models and CFD results. At each time step, the forces from each component are calculated based on the state variables, and the net forces and moments are summed up.

4.3.1 Sail Model

The sail set of *Linnea* consists of the Mainsail and a jib for upwind sailing and an additional Jib0 for downwind sailing. Sails are modelled using the VPP guide by the Offshore Racing Congress (ORC VPP Documentation, 2019). Sail depowering is achieved by the use of two parameters: *flat* and *reef*. *Flat* determines the lift coefficient of the sails and *reef* determines the area of the sails. For better performance, the *reef* is not reduced until the minimum value of the *flat* parameter is achieved, and depowering is done only after the sailors are fully out on the racks.

4.3.2 Hull Model

Acerbi et al (2017) carried out CFD tests on *Linnea's* hull for different speeds which were available to be implemented in the DVPP. The change of frictional hull resistance with the draft of the boat is assumed to be proportional to the wetted surface area. Based on the Delft systematic yacht series, the change in wave-making resistance is assumed to be proportional to the change in displacement (Gerritsma et al, 1981). The mass and moment of inertia of the hull were obtained by weighing the hull and through a swing test. Inertias due to the rigging and other small components are estimated using inertia formulae for simple geometries, adding it together with Huygens–Steiner theorem.

4.3.3 Foil Model

Foils and the appendages are modelled using the Lanchester–Prandtl lifting line theory. For elliptical loading and sufficiently high aspect ratio (AR) the following formulas hold

$$C_{L,3D} = \frac{C_{L,2D}}{1 + \frac{2}{AR_e}} \tag{10}$$

$$C_{D,i} = \frac{C_{L,3D}^2}{\pi AR_e} \tag{11}$$

11

Almost elliptical loading is obtained with a taper ratio (TR) of 0.45. For an aspect ratio of around 8 the induced drag from equation 11 is then accurate within 1% (Larsson et al, 2014)

Simulations from X-Foil (Drela and Youngren, 2013) provided the 2-dimensional force coefficients for the appendage sections as a function of the angle of attack, the flap angle, and the Reynolds number. Figure 9 shows the computed 2D lift coefficients as a function of flap angle and angle of attack.
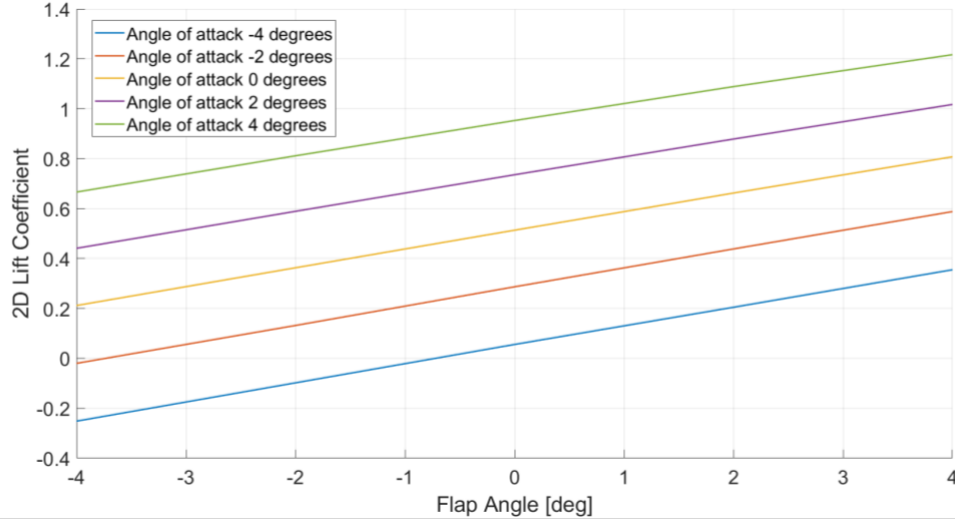

Figure 9. 2D Lift coefficient vs flap angle for different angles of attack

Equations 10 and 11 are based on the effective aspect ratio, AR_e, which is the geometric AR of the wing if the wing has two free tips in the flow. If one end of the wing is fixed such that no overflow is possible, AR_e is twice the geometric AR.

In case of the split TE flaps at different deflection angles, since the loading on the starboard and port sides are different, each side is treated as a separate wing with half the span. If there had been an infinitely large plate in the symmetry plane between the two wings halves, the AR_e would be doubled for each half-wing and the effect the same as having a full wing (figure 10). In practice, there is an overflow between the two flaps at different deflections, so the increase in AR_e would be smaller. Treating the interface as a free tip would reduce the AR_e to the actual geometric AR of the half-wing. To obtain a more exact AR_e, CFD computations were carried out, as reported in section 5.
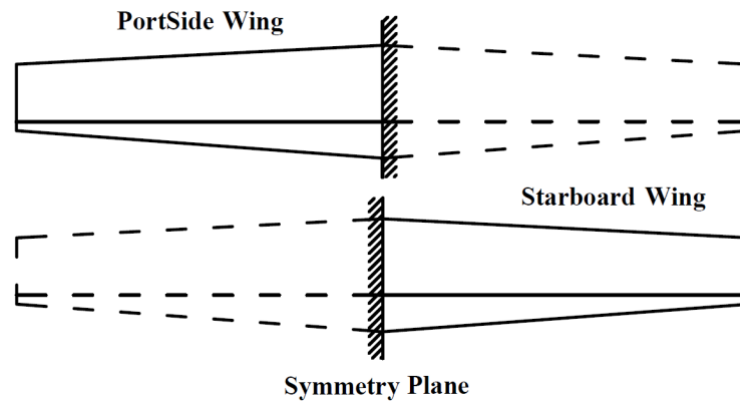

Figure 10. Port and starboard foil considered as separate wings with a symmetry plane on the centreline

As the foil approaches the free surface, the negative pressure on the upper part of the foil interacts with the free surface, thereby deforming it (Hoerner and Borst, 1975). The deformation of the free surface reduces the negative pressure on the suction side of the foil, thereby reducing the lift coefficient. Faltinsen (2005) has determined the loss of lift coefficient as a function of the submergence Froude number and foil chord. Figure 11 shows the variation of the 2D lift coefficient with the submergence compared to the C_L at infinite depth for the Wortmann FX60100.
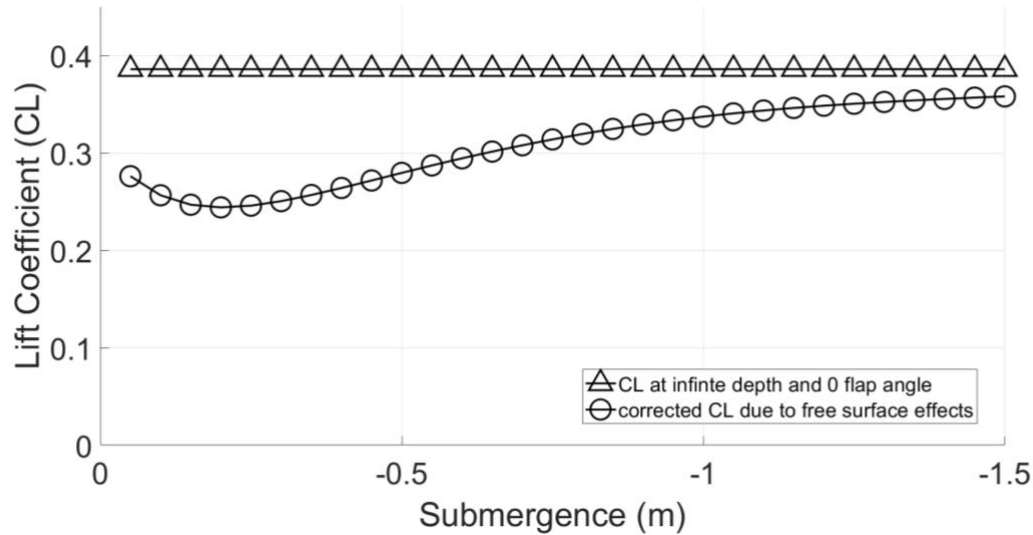
Figure 11. 2D lift coefficient as a function of foil submergence

With the foils close to the free surface, there is also an increase in the induced drag. Due to the finite span of the foils, the fluid dynamic properties of the foil close to the free surface are similar to that of the lower wing of a biplane (Hoerner, 1957). The AR_e is multiplied by a factor of K, computed by Hoerner (figure 12), which takes a value between 1 and 2 for the biplane wings for T-foils. For a box plane, the K factor is much lower between 0.5 and 2, significantly reducing induced drag.
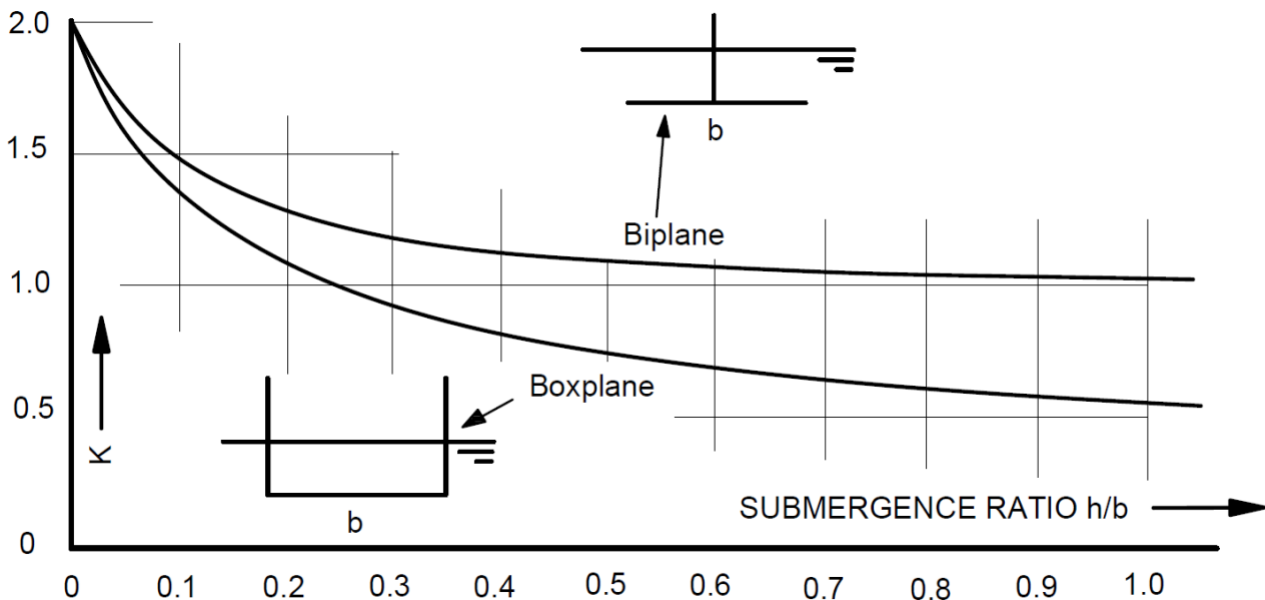

Figure 12. Induced resistance factor K as a function of submergence ratio (Hoerner, 1957)

13

4.4 Control System Design

Control systems are modelled as response equations that return the flap angle (f) as a function of the state variables: ride height (h) and heel (φ). Ride height is the displacement of the yacht in the body coordinate system (a measure of the displacement of the wand).

4.4.1 Two-Wand System (AHSS)

The two-wand system is designed to automatically adjust the port and starboard flap angle based on the ride height and heel angle of the boat. With a single wand, a response curve would be as in equation 12. The response of the flap angle to the change in height, i.e., the slope of the ride height vs flap angle curve, termed as a gain coefficient (GC), is quite critical to ensure a stable ride. A low slope system would be less sensitive to disturbances, but it would reduce the flaps at a lower rate with the h. This would result in a higher h at equilibrium. Whereas a high slope system would reduce the flap angle rapidly with ride height and result in a lower hull clearance, with high sensitivity to disturbances. h is negative upwards in the body coordinate system.

$$f = GC * \frac{h}{0.681} + f_o \tag{12}$$

In the two-wand system, the heel angle is implicitly measured as the difference in ride height at the port and starboard extremes (where the wands are located). Equation 12 is applied for each wand, with h being the height measured at the respective wandThe flap angles at port and starboard, f_s and f_p, are given by equations 13 and 14, where b is the maximum beam of the yacht. The response equations are linear since the variation of lift coefficient with the flap angle is linear (figure 9) for this foil. Linear response curves will ensure that the total $C_{L,2D}$ is kept constant when heeling, since the loss on one side is the same as the gain on the other side. φ is negative with a starboard heel.

$$f_s = GC * \frac{(h - b * 0.5 * \tan(\varphi))}{0.681} + f_o \tag{13}$$

$$f_p = GC * \frac{(h + b * 0.5 * \tan(\varphi))}{0.681} + f_o \tag{14}$$

The gain coefficient (GC) in equations 13 and 14 determines both the height- and heel-response of the control system because heel cannot be directly measured with the two-wand system. If GC is increased, the difference in the flap angles for a given heel angle is increased, thereby producing a larger righting moment. However, the response to a change in ride height would also be larger and it could result in a lower stable ride height. Sensitivity to the GC is studied in section 6.1.

The optimal initial flap angle (f_o) when the hull is fully submerged is also critical in determining the take-off speed of the boat. A high initial angle would generate a high lift at the cost of increased profile and induced drag. Thus, the optimal value for the lowest take-off TWS was found to be +5 degrees using the static VPP.

4.4.2 Performance Control – Manual Offset System

For producing a manual offset the same response curves in equations 13 and 14 are used with an additional $offset$ term. The $offset$ is controlled by the sailors during the race, increasing the offset to produce an additional righting moment.

$$f_s = GC * \frac{(h - b * 0.5 * \tan(\varphi))}{0.681} + f_o + offset \tag{15}$$

$$f_p = GC * \frac{(h + b * 0.5 * \tan(\varphi))}{0.681} + f_o - offset \qquad (16)$$

4.5 Sailor Model

To run dynamic simulations, automated PID controllers are modelled to reflect practical sailing by adjusting the Transverse Centre of Gravity (TCG) of the sailors and the $flat$ and $reef$ of the sails. The rate of change of these variables is dependent on multiple parameters such as the heel angle (φ), roll angular velocity (p), and force on the sails (equations 17, 18, and 19).

$$\Delta TCG = SRC \left(Kc_{11}\varphi - Kc_{12} \, SailForce - Kc_{13} \, p \right) \qquad (17)$$

$$\Delta flat = SRC \left(Kc_{21}\varphi - Kc_{22} \, SailForce - Kc_{23} \, p \right) \qquad (18)$$

$$\Delta reef = SRC \left(Kc_{31}\varphi - Kc_{32} \, SailForce - Kc_{33} \, p \right) \qquad (19)$$

The coefficients Kc are optimized for ideal sailing conditions by an iterative process using the DVPP. Till the sailors are fully out on the racks, $\Delta flat$ and $\Delta reef$ are set to zero. SRC is the sailor response coefficient and is a measure of the effectiveness of the sailors to react to a disturbance.

5. CFD STUDY OF THE INDUCED DRAG DUE TO THE SPLIT FLAPS

As explained in section 4.3.3, the split flaps generate additional induced resistance. Looking at this in more detail, while heeling to starboard, the two flaps are set at different angles as shown in figure 1 with a higher flap angle on the starboard side. This implies that the $C_{L,2D}$ will be higher on the starboard side of the foil than the port side. In such conditions, due to the space between the two flaps in the middle, additional vortices will develop, leading to increased drag. Due to the higher loading on the starboard side, the tip vortex will be much stronger than the port side. The flow in the space between the flaps is complicated as it facilitates a partial overflow from the pressure side to the suction side. On the starboard side, the overflow will be much stronger due to the higher wing loading. Whereas, on the port side, the overflow will be weaker or even in the opposite direction if the $C_{L,2D}$ is negative.

The above effects were studied with numerical RANS simulations to correct the AR_e. Friendship Systems CAESES (2019) was used to make the CAD model of the foils and Star CCM + (2018) was used to carry out the CFD simulations. The $k - \omega$ turbulence model was used with the foils in a double body setup. Numerical verification was done using the foil of an A-Class catamaran and comparing it against experimental results from Keller et al (2017).

The simulations were carried out at a constant speed of 5 m/s by setting the difference between the flap angles (f_{diff}) as the critical parameter. f_{diff} was varied from 0 to 4, 8, 12, and 16 degrees as in table 1.

$$f_{diff} = |f_s - f_p| \qquad (20)$$

Empirical results are made with the assumption that the AR_e for the half wing is doubled, and hence might underpredict the induced drag. As the friction drag is not of concern in this study, only the drag due to the pressure effects are considered. The total pressure drag in the empirical method is estimated as the sum of the profile pressure drag and lift induced drag. The results from the numerical simulations are compared with empirical estimations in Table 1 and Figure 13. The black dashed curve represents the CFD results for symmetrically deflected flaps, i.e., where the starboard

and port flaps are displaced equally much from 0, but in different directions and the red curve represents the empirical model. The yellow curve includes a correction to the empirical method, such that the empirical formula fits the CFD results as well as possible.

This correction is added to the AR_e DVPP to account for the increased resistance due to the split-flaps. The correction factor (C_{AR}) on the aspect ratio is given by the equations 21 and 22. Note that this correction is derived from the symmetric displacement of the flaps. To cover also asymmetric deflection more CFD results are required, and this is a matter for further study.

$$C_{AR} = 1.9338 * f_{diff} - 2.0332 \tag{21}$$

$$AR_C = AR * \left(1 - \frac{C_{AR}}{100}\right) \tag{22}$$

Table 1. Comparison of the empirical and numerical pressure drag for flap differentials of 0, 4, 8, 12, and 16 degrees.

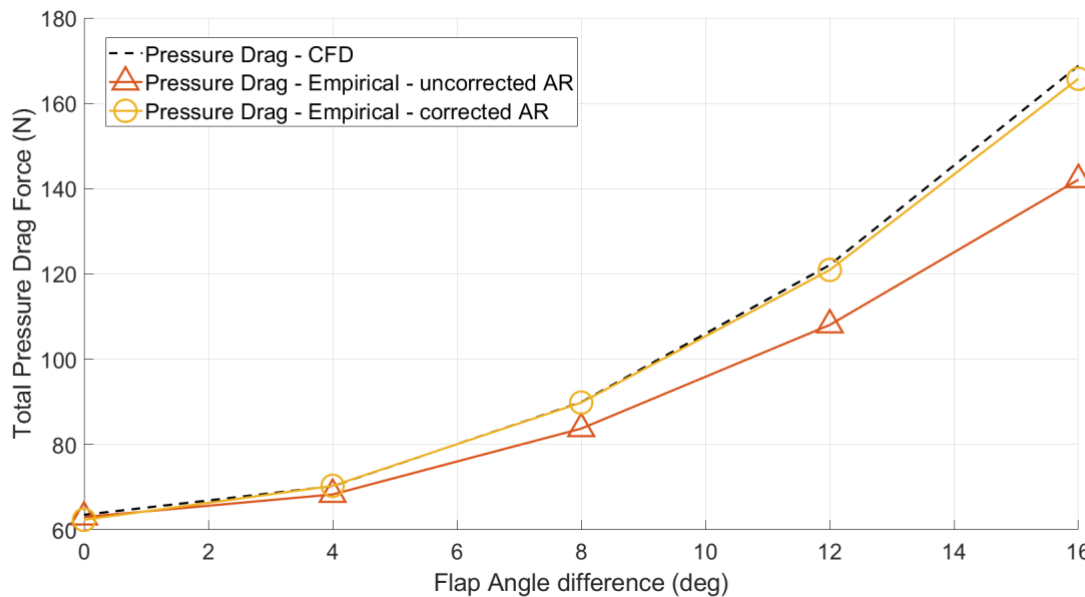| Flap Difference (deg)	f_P	f_S	Empirical Pressure Drag (N) without AR correction	Empirical Pressure Drag (N) with AR correction	CFD Pressure Drag(N)
0	0	0	63	63	64
4	-2	2	68	70	70
8	-4	4	84	90	90
12	-6	6	108	121	122
16	-8	8	142	166	169

Figure 13. Pressure drag force vs flap angle difference for empirical and CFD estimations

Figure 14 shows streamlines in the space between the two flaps with a f_{diff} of 16 degrees. From Figure 14, it can be seen that there is an additional vortex developed at the space between the flaps, which contributes to the discrepancy between the CFD and empirical methods. The difference in the pressure distribution between the starboard and port sides due to the f_{diff} can be seen in figure 15.
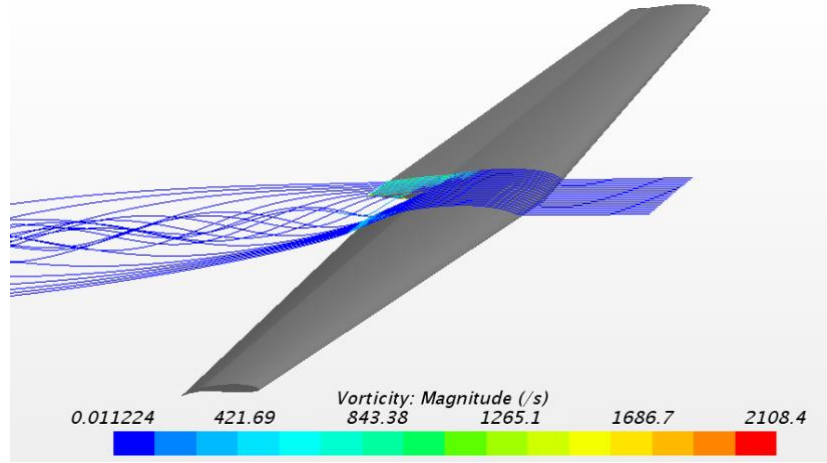
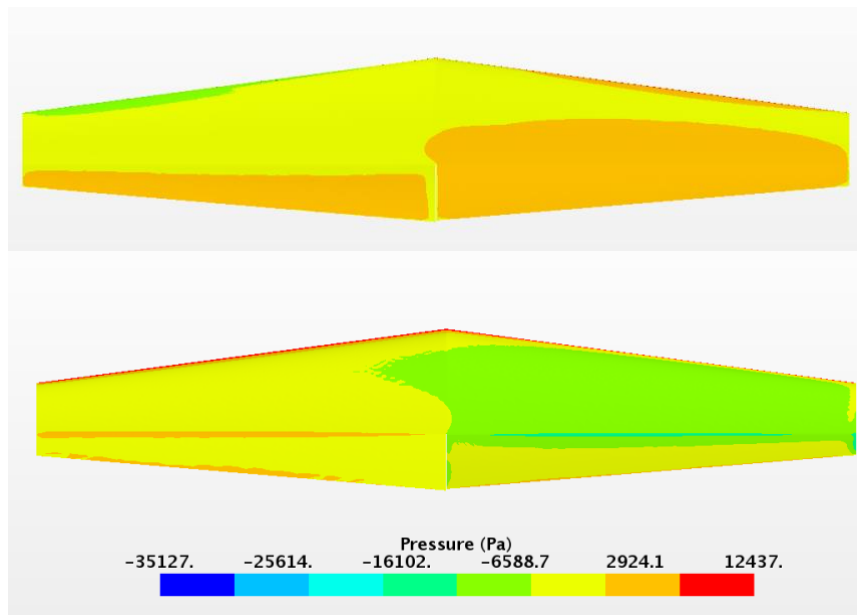**Figure 14 streamlines the interface between the split flaps**

Figure 15. Pressure contours on the pressure side (top figure) and suction side (bottom figure) with the starboard flaps (right) set at +8 degrees and port flaps (left) set at -8 degrees

To study the interaction effects in detail, two additional simulations were carried out with the starboard flap set at 0 degrees and the port flap set at -3 degrees and -10.7 degrees. Flap angle of -3 degrees and -10.7 degrees has a $C_{L,2D}$ of 0.2866 and -0.2866 respectively. Theoretically, the induced drag is proportional to C_L^2 and hence the empirical $C_{D,i}$ should be the same for both cases. The results from the numerical and empirical simulations are given in table 2.

From table 2, due to the discrepancy between the empirical and numerical methods, it is seen that there is a strong interference effect between the two sides when the port and starboard flaps are set at 0 and -10.7 degrees, respectively. Figures 16 and 17 show the velocity vectors on the transverse plane at the trailing edge of the foil viewed from behind for case 1 and case 2, respectively. The plots are enlarged closer to the space between the two flaps.

17

Table 2. Comparison of the empirical and numerical pressure drag for a starboard flap of 0 degrees and a port flap at -3 and -10.7 degrees.

Case	1	2
Starboard Flap (deg)	0	0
Port Flap (deg)	-3	-10.7
Empirical Pressure Drag (N)	44	54
Numerical Pressure Drag (N)	46	61
Empirical Lift (N)	2444	657
Numerical Lift (N)	2404	565

In case 1, there was no strong vortex formation in the space between the flaps (figure 16). There is a lack of space for vortex formation as each flap hinders the overflow from the other flap to some extent. Also, both flaps are loaded positively with pressure on the bottom and suction on the top. Thus, on the starboard side, the overflow from pressure to suction side would tend to roll clockwise in the space between the flaps. On the port side, the overflow tends to roll in the counterclockwise direction. These two flows seem to oppose each other and could hinder the formation of a stronger vortex.
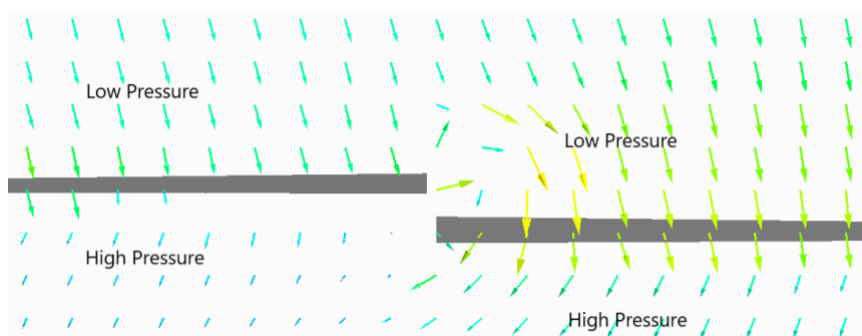

Figure 16. Velocity vectors at the Trailing Edge of the foil with starboard flap at 0 degrees and port flap at -3 degrees (case 1) – viewed from behind

In case 2 (figure 17), the vortex in the space between the flaps is much stronger than in case 1. The space between the flaps is larger due to the large f_{diff}, aiding is unhindered vortex formation. Since the loading on the port side is negative i.e., high pressure on the top and low pressure on the bottom due to the negative lift coefficient, the overflow on the port side will roll up clockwise in the space between the flaps. The starboard overflow also rolls clockwise due to the positive loading, and these two flows seem to complement each other, contributing to a stronger vortex in the space between the flaps.
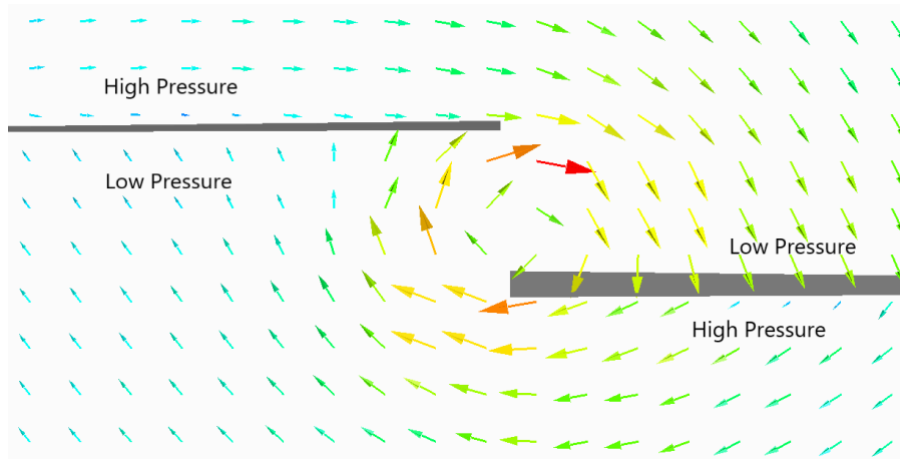
18

Figure 17. Velocity vectors at the Trailing Edge of the foil with starboard flaps at 0 degrees and port flaps at -10.7 deg (case 2) – viewed from behind

Though in both cases the starboard flap is at the same angle, the pressure below the flap has been significantly reduced in case 2 due to the stronger vortex. This contributes to a reduction in the lift coefficient as well. The correlation error between the numerical and empirical estimations for case 2 is significantly larger than for case 1 and all other simulations represented in table 1. The errors in the pressure drag and lift estimations are 12.9 % and -14.0 % respectively.

The case with +8 starboard and -8 port flaps has an error of 1.7 % on the pressure drag. Though the f_{diff} here is larger than case 2, the correlation is better. This could be attributed to the fact that a port flap of -8 degrees corresponds to an approximately zero (slightly negative) lift coefficient. The starboard flap at 8 degrees has a positive lift coefficient and would produce a vortex that rolls up clockwise in the space between the flaps. There would be no significant vortex formed from the port side and thus no complimentary effect to the clockwise port flap vortex. Therefore, it could be inferred that it is not only the difference between the flap angles (f_{diff}) but also the loading patterns of the two flaps, which is critical in increasing the pressure drag. As observed from the studies, a negative loading on one of the flaps strengthens the vortex in the space between the flaps and a non-negative loading on both the flaps tends to weaken the vortex.

6. RESULTS

6.1 Increase in Righting Moment due to the Split-Flaps

In the case of the AHSS, the gain coefficient (GC) determines both the heel and ride height stability (Equations 13 and 14), with a higher GC a large response to a given change in height and heel, reducing the ride height (h) and increasing the Righting Moment (RM). With a constant f_{diff}, the righting moment is proportional to the square of the boat speed. Figure 18 shows the righting moments for a GC of 8, 12, and 16, respectively at a leeward heel of 10 degrees as a function of boat speed. The righting moment of the fully displaced hull is also shown in figure 18. Over a large part of the speed range, the foil-supported boat has a higher RM than the displacement boat when a gain coefficient of 12 is used. With a gain coefficient of 16, the RM is higher than the displacement boat for the entire range of speeds.

The reduction of RM at higher speeds in figure 18 is attributed to the negative limit of -7 degrees on the flap angle. At high h or high heels, one or both the TE flaps can reach the minimum limit. Figure 19 shows the flap angles at each speed for the different GC at a heel of 10 degrees to leeward. With a high GC, the net flap angle is lower than with a lower GC at the same h. Heeling with an already low net flap angle reduces the windward side's flap angle even further and it reaches the negative limit of -7 degrees rapidly. Heeling further will increase the righting moment at a lower rate as the

windward flap is locked at -7 degrees and only the leeward flap increases. If the speed increases in such a case, the net h increases, thereby decreasing the net flap angle. As the windward side is already set at -7 degrees, only the leeward side can be decreased, thereby decreasing the difference between the flap angles. This explains the reduction of RM at high speeds and high GC.
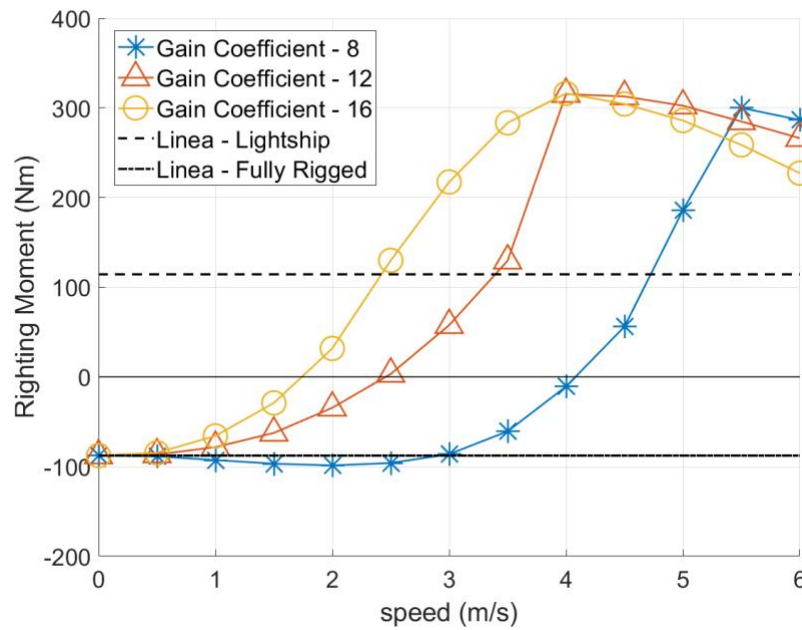

Figure 18. Righting Moment of Linnea due to the foils for a draft of 1.0 m and gain coefficients of 8, 12, and 16 and a heel of 10 degrees to leeward
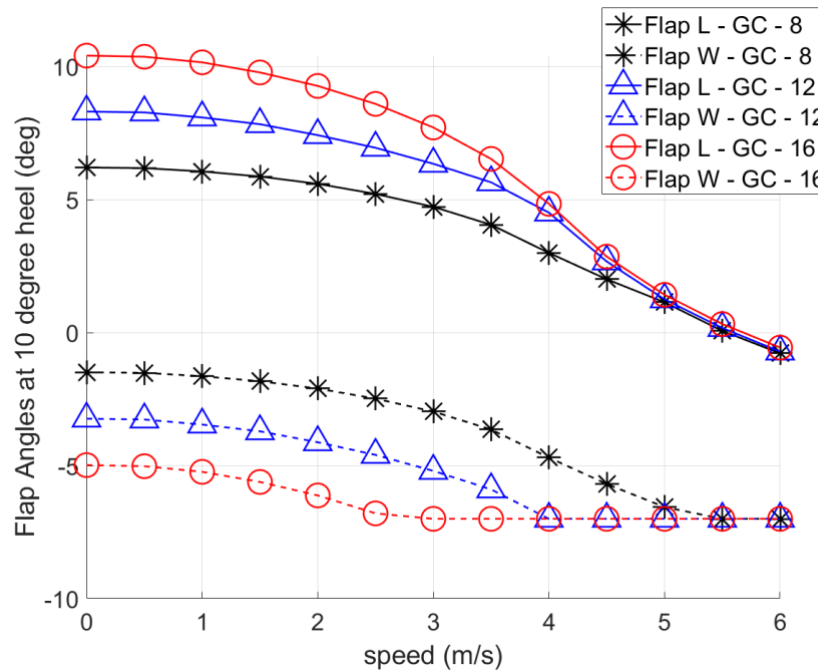
Figure 19. Flap angles versus speed with the different gain coefficients of 8, 12, and 16 at a heel angle of 10 degrees to leeward

The above issue could be resolved by removing the negative limit on the flap angle. This solution would result in two complications. One would be that the windward side will be producing negative lift, which is a loss of efficiency. The two sides would then generate forces in the opposite directions and the total lift induced resistance would be large. Another effect is that a high righting moment will increase the load on the rigging. To manage the high loads, the rigging strength would have to be increased, leading to a higher weight, moving the CG upwards. A higher CG would increase the heeling moment, possibly negating the increased RM from the split-flap system. For these reasons, the negative limit is retained.

6.2 Effectiveness of the Stability Control System

The effectiveness of the AHSS is studied using gust simulations (increase in the True Wind Speed, TWS) keeping the True Wind Angle (TWA) constant. Equilibrium conditions are estimated using the DVPP at a TWS of 3.5 m/s and a TWA of 60 degrees. As *Linnea* is designed for lighter winds, foiling is achieved at such low wind speeds. Two gust scenarios are simulated: a lighter gust for a long duration and a stronger gust for a short duration. Figure 20 shows the TWS as a function of time for the two gust scenarios.
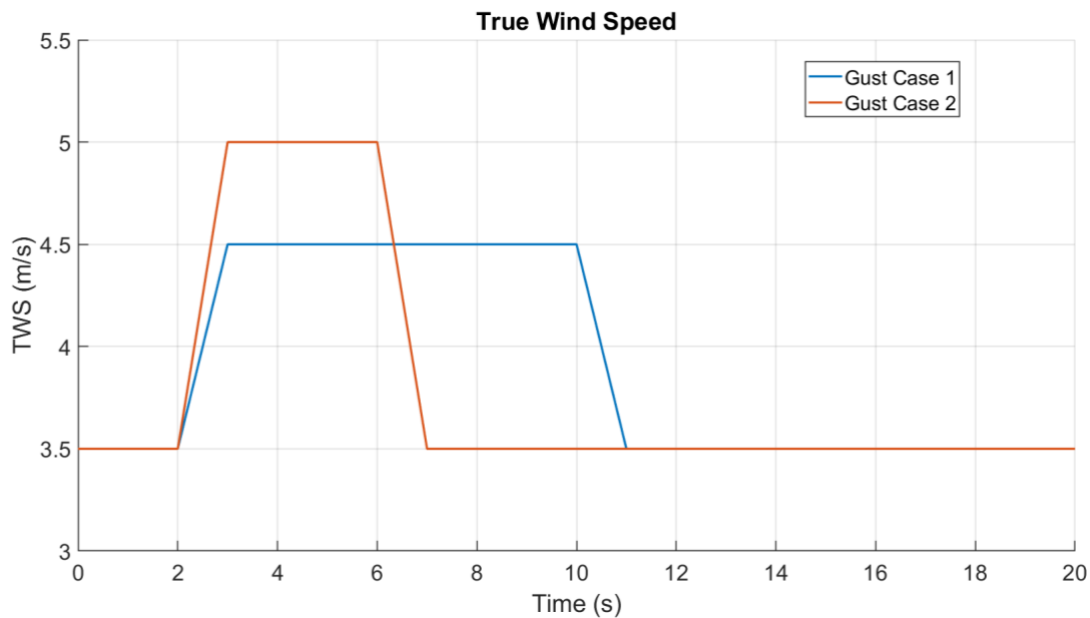

Figure 20. Gust scenarios simulated using the DVPP

The heel response of the boat to the lighter gust (case 1) in degrees is shown in figure 21. A negative heel represents a heel to starboard (leeward side). As the TWS increases, the boat starts to heel to leeward due to the increased heeling moment of the sails, and as the gust is reduced the boat reverts back to its original sailing state. The boat without the split flaps heels much more than the boat with AHSS. Increasing the gain coefficient significantly reduces the heeling angle during the gust and returns the system to equilibrium quicker. Oscillations in the curves are due to the sailor control system.
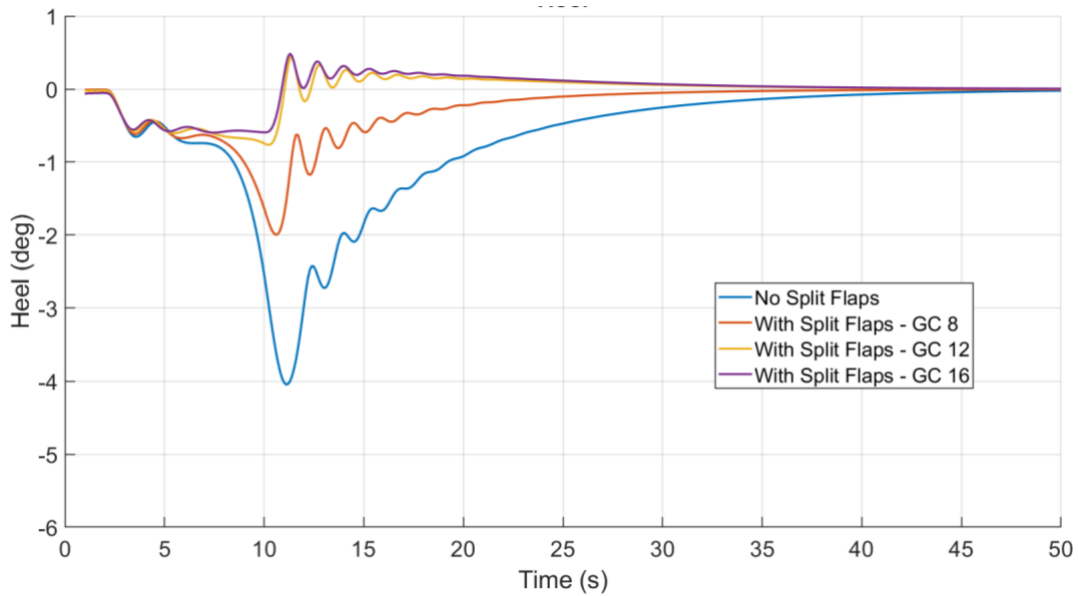
Figure 21. Heel angle of the boat during the lighter gust (gust case 1)

In a stronger gust (case 2), the boat naturally heels more. See figure 22. The boat without AHSS capsizes under the heavy load on the sails. With the AHSS, the boat does not capsize and can return to the equilibrium state after the disturbance is removed. A gain coefficient of 8 of the AHSS limits the heel to leeward to 14 degrees during a strong gust. Increasing the GC to 16, the heel angle is limited to just 3.75 degrees. It could be inferred that, with the two-wand system, the AHSS is capable of stabilising the system considerably during gusts.
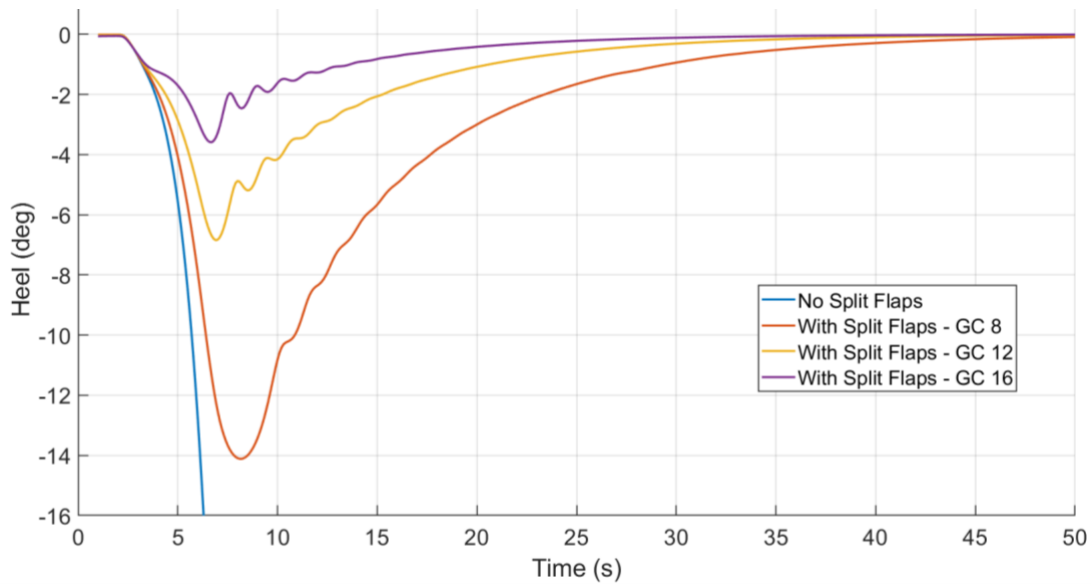

Figure 22. Heel angle of the boat during the stronger gust (case 2)

Figures 23 and 24 show the boat speed during the gust scenarios. During the race, it is instrumental to minimize speed loss. With the TWS increase, boat speed increases, and once the disturbance is removed, there is a drop in boat speed. With the AHSS, the boat returns to the original sailing state without any significant loss of boat speed after the disturbance is removed. The AHSS boat experiences a relative increase in the boat speed attained during the light gust compared to the boat without the split flaps (figure 23).
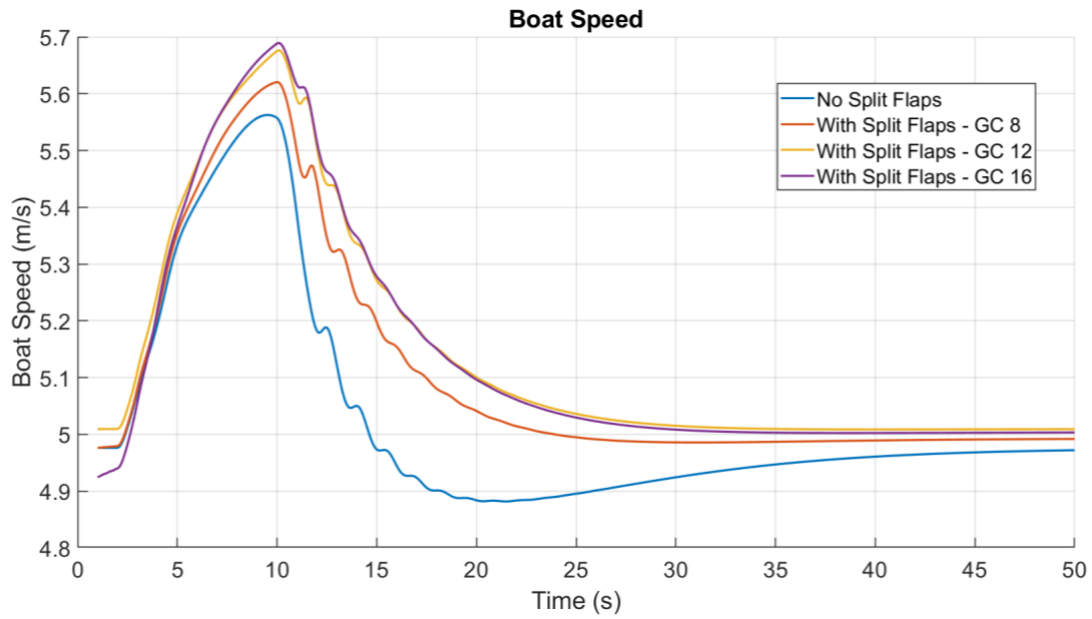
22

Figure 23. Boat Speed during the lighter gust (case 1)

In the case of a stronger gust (case 2), the AHSS with a GC of 8 experiences a significant speed drop after the gust. With larger GC: 12 and 16, the drop in speed is significantly reduced, which also provides a performance advantage amid the race (figure 24) along with increased stability.
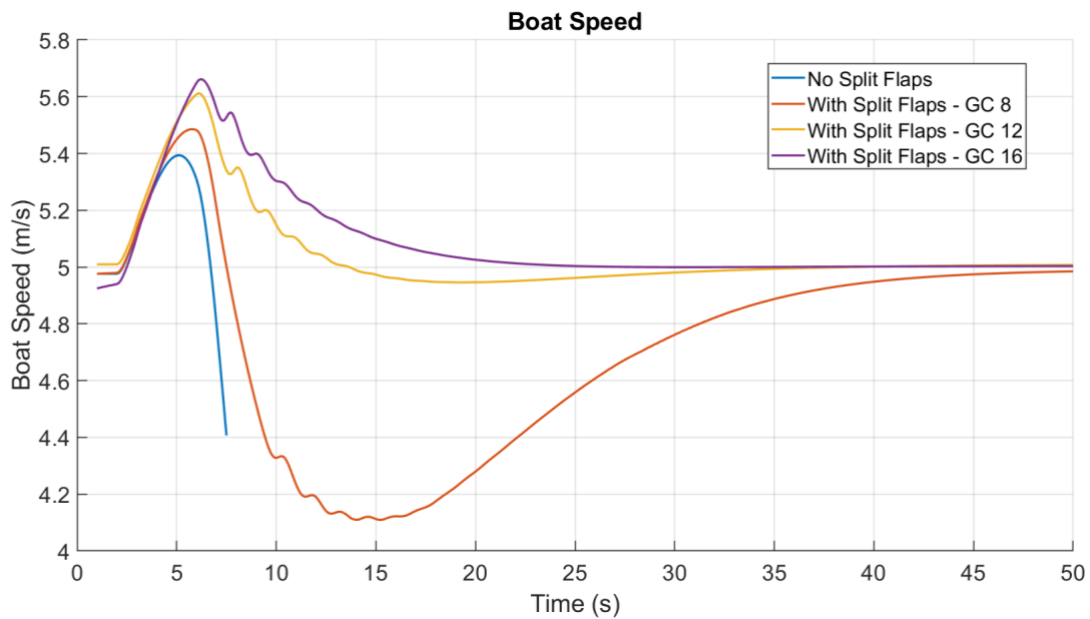

Figure 24. Boat Speed during the stronger gust (case 2)

Using a GC of 8, the boat heels significantly with a strong gust. Although it performs better than the boat without the split flaps, the large heel might be challenging for the crew to tackle. Hence it might be better to use higher gain coefficients greater than 8. With a GC of 16, the boat is very stable in gusts and does not lose speed due to disturbances. However, since the two-wand system is used here, a higher GC will have an impact on the ride height. As seen in figure 25, the stable ride height of the boat with the higher GC is significantly lower than with a GC of 8. The black dashed line represents the ride height at which the lowest part of the hull leaves the water surface. Thus, with a GC of 16, the hull clearance is around just 4 cm, which could be sensitive to the impact of waves.

23

The reduction of ride height is a consequence of using the two-wand control system as a higher GC reduces the flap angle at a higher rate for an increase in the ride height. This drawback of the two-wand system limits the usage of higher GC and thereby reduces the stability of the boat.
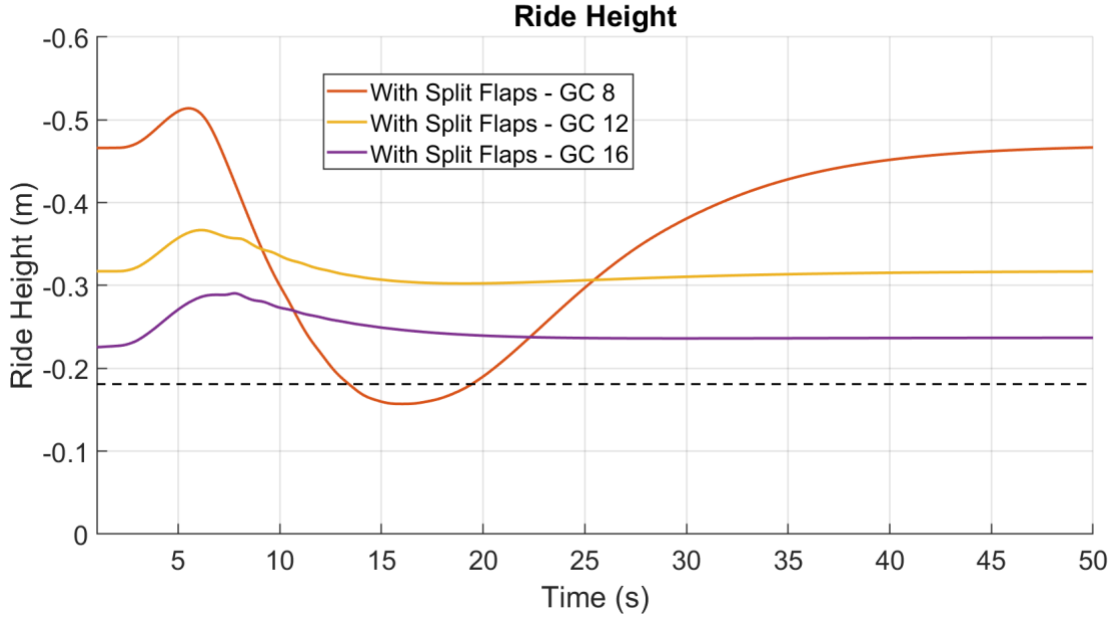

Figure 25. Ride Height during the stronger gust (case 2)

6.2.1 Decoupled Ride Height-Heel

To effectively increase the righting moment without affecting the ride height, the heel and height measures need to be separated and the flaps should be adjusted accordingly with different gains. Mathematically such a system would behave according to equations 23 and 24, which are modified from equations 15 and 16, separating height and heel angle φ, adjusting them proportional to GC_{height} and GC_{heel} respectively.

$$f_s = \frac{GC_{height} * h - GC_{heel} * \varphi}{0.681} + f_o + offset \qquad (23)$$

$$f_p = \frac{GC_{height} * h + GC_{heel} * \varphi}{0.681} + f_o + offset \qquad (24)$$

Such a system measures the heel angle explicitly, allowing for a higher gain on the heel without compromising the height response. By increasing GC_{heel} to 16 while retaining GC_{height} at 8, the heel stability of the boat could be significantly increased without reducing the ride height. Figure 26 shows the ride height of the boat with the decoupled ride height-heel system during the stronger gust (case 2). The system with $GC_{height} = 8$ and $GC_{heel} = 8$ behaves similar to the two-wand system, which is expected according to equations 23 and 24. By only increasing the GC_{heel}, the heel stability of the boat can be increased significantly. As seen in figure 26, the stable ride height is the same for all the plots as the value of GC_{height} remains unchanged. Thereby increasing the heel stability without affecting the ride height of the boat.
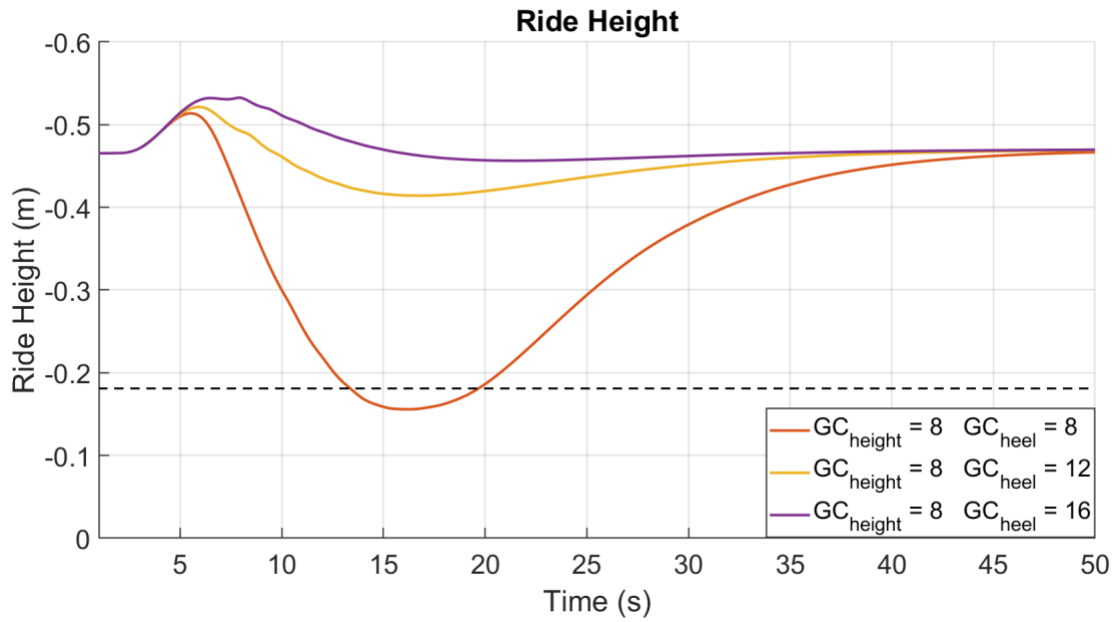
24

Figure 26. Ride Height during the stronger gust (case 2) with the decoupled system

The decoupled control could be achieved with electrical sensors and computers that could split the heel and height signals, and proportionally adjust the flaps. However, many classes including the R3 class rules prohibit the use of stored power onboard, limiting the use of electronics. Hence a mechanical system that could decouple the ride height and heel system has been developed and is presented in section 7.

6.3 Effectiveness of the Manual Offset System

Heeling windward increases the righting moment due to the gravity forces, which allows to power the sails more, resulting in a faster boat (figure 27). The AHSS, which automatically adjusts the flap angles with the heel angle, will oppose heeling to windward by increasing the windward flaps and producing an additional heeling moment. The manual offset system introduces an $offset$ parameter in the control system. By increasing the $offset$ value, the windward flap angle can be decreased, increasing the leeward flap angle by the same amount. Thereby, the effects of the AHSS are negated and the foil could create a righting moment towards windward despite the windward heel.

Figure 27 shows the boat speed from rest to compare the efficiency of the offset system during a windward heel of 10 degrees. It can be seen in figure 27 that the AHSS reduces the boat speed with a windward heel due to the heeling moment produced (sails would be depowered). By increasing the $offset$ to 2.2 degrees, the effects of the AHSS will be neglected and the difference between flap angles will be zero. With an $offset$ of 4.2 degrees, f_{diff} of 4 degrees, the boat speed with AHSS is increased relative to the boat without the split-flaps. Further increasing it to 6.2 degrees, the boat becomes even faster (figure 27) despite the increase in induced resistance.

With the manual offset system, one of the drawbacks of the AHSS that is the inability to sail with a windward heel could be negated. The system now has a performance advantage and increased heel stability due to the AHSS with the manual offset.
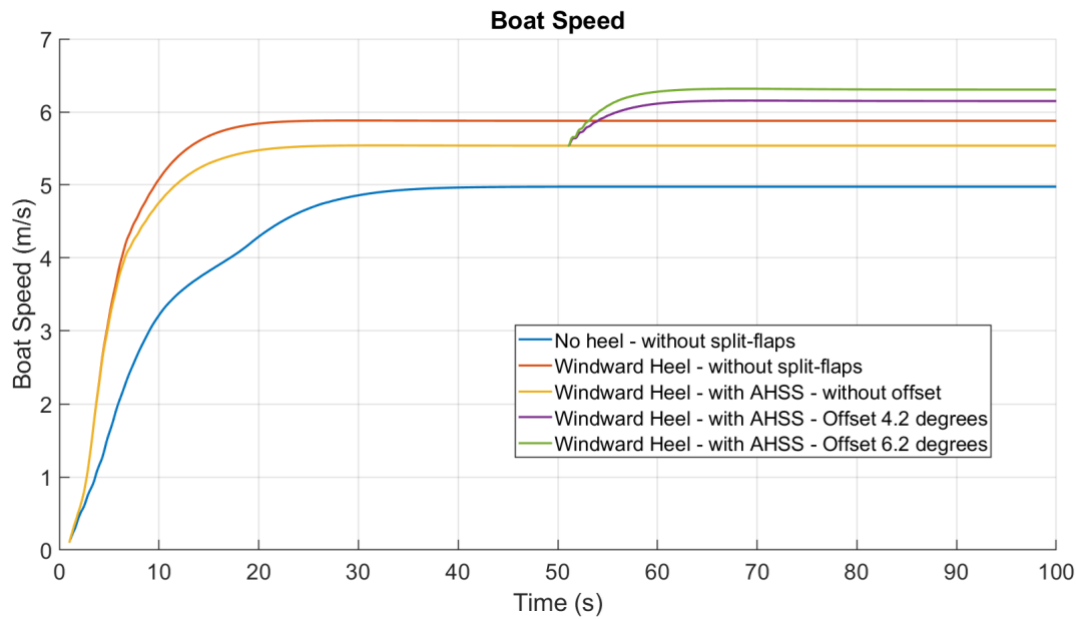
Figure 27. The performance advantage of the manual offset system

7. DECOUPLED RIDE HEIGHT-HEEL MECHANICAL CONTROL SYSTEM FOR SPLIT FLAPS

The dual wand control system presented above compounds ride height and heel in a composite signal, meaning that the same gain will be applied to both. If the ride height and heel instead could be measured as separate signals, in a decoupled fashion, individual gains can be applied to the ride height and heel signals, potentially improving the performance of the control system and the boat.

In this work, a mechanical system that allows the ride height and heel signals to be separated has been devised. The system consists of a measurement system, which measures ride height and heel separately, and a control cam system which applies individual control laws to the two signals and output individual port-starboard flap deflection angles.

The system uses two rigidly connected wands, positioned in an inverted-V shape. Similar to the control systems typically used on in the International Moth Class, the wands are connected to a cam, and allowed to rotate around a transverse axis at the end of the bowsprit, see Fig. 28, point 1. This translates the ride height measurement of the wands to a translation in a pushrod that runs along the centre of the bowsprit, see Fig. 28, point 2.
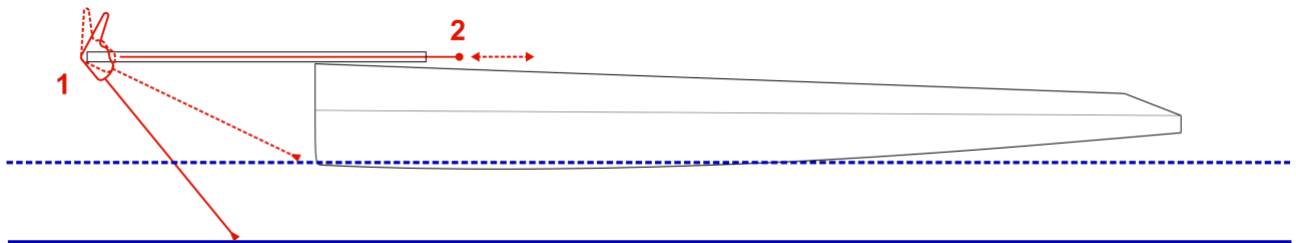

Figure 28. Decoupled control system response to change in ride height

The entire wand-cam assembly is also allowed to rotate around the longitudinal axis of the bowsprit, in relation to the boat and bowsprit. The inverted-V configuration and resulting lateral separation of the wand paddles mean that the wand assembly will remain aligned with the free surface as the boat heels. In this way the heel of the boat is measured by the rotation of the wand-cam assembly, see figure 29.
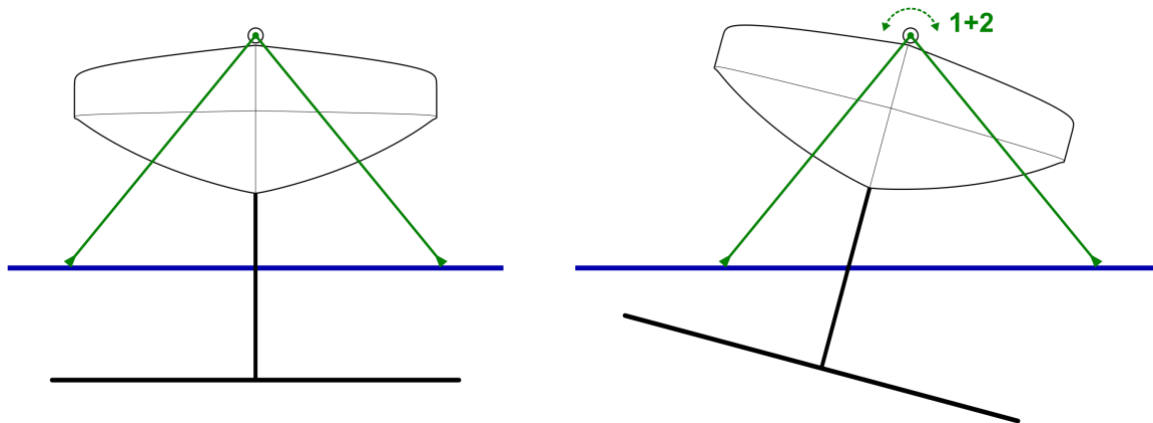
26

Figure 29. Decoupled control system response to change in heel angle

The forward end of the pushrod shaft is connected to the wand-cam assembly with splines, which allows torque to be transferred while still allowing relative translation. In this way, the wands can measure and transfer ride height and heel signals separately, as pushrod translation and rotation.

The control-cam assembly uses a globoid 3D cam to apply individual control laws to ride height and heel signals, transforming these to individual port and starboard flap deflection signals. The globoid cam can be described as a generalized cylinder, with varying cross-section. It is rigidly connected to the end of the pushrod, rotating and translating with it. The change in diameter along the length of the cam defines the control law for ride height, while the cross-section shape defines the control law for heel. Two individual flap pushrod followers ride on the cam surface, transmitting the signal to each flap. The response of the control-cam assembly to ride height and heel signals is shown in Figures 30a and 30b.
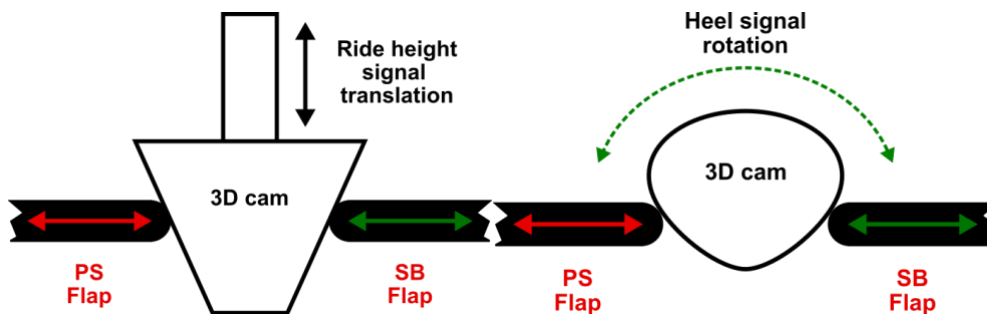

Figure 30. Control cam and flap pushrod followers– (a) Top view, response to ride height signal (b) Axial view, response to heel signal

From Figure 30a, it can be realized that a change in ride height, which leads to a longitudinal translation of the 3D cam, results in an equal change in port-starboard flap angles, thus changing the total lift produced by the foils without affecting righting moment. Note that, while the cam design results in a linear response to ride height, arbitrary control laws could be implemented by changing the cam shape.

From Figure 30b, it can be realized that a change in heel, which leads to rotation of the cam around the longitudinal axis, will result in differential flap angle, increasing the flap angle on one side, while reducing the other. With careful design of the cam shape, this means that righting moment can be generated, without affecting total lift.

As shown in section 6.3, manual heel offset can provide increased performance. Such an offset function can be added to this system, by rotating the 3D control cam in relation to the pushrod shaft.

27

CONCLUSIONS

Dinghies supported by T-foils are inherently unstable, but by splitting a trailing edge flap into starboard and port flaps, the transverse stability is greatly improved. The split-flap control system, Automated Heel Stability System (AHSS) adjusts the flap angle difference in proportion to the heel angle, thereby increasing the transverse stability of the boat.

When the boat heels to leeward, the gravity forces produce a heeling moment, and hence windward heeling is preferred to increase the arm of the gravity force. The AHSS would oppose windward sailing and a manual offset system (complimenting the AHSS) may be used to adjust the flaps to produce a righting moment whilst heeling windward.

The extreme skiff (*Linnea*) was investigated as a demonstration case for the split flaps in this study. *Linnea* is studied using a developed DVPP with the AHSS and the manual offset system. For the AHSS, a two-wand mechanical control system is used to measure and adjust flap angles based on height and heel by responding to the height at the maximum beam on both sides. The flap control system is modelled in the computations using response functions to transfer the changes in ride height to the flaps.

The gain coefficient, which is the slope of the height-flap response curve is a critical parameter for transverse stability. Evaluations show that, with a proper design, the split-flaps can increase the righting moment more than the displacement hull without foils. Since the GC is coupled with the height also, a large gain coefficient results in a much lower ride height. Decoupling the ride height and heel results allows increasing the gain on the heel while maintaining a low gain on the ride height. The mechanical design of such a system could be achieved with a V-shaped wand and a globoid cam.

A systematic CFD investigation of the flow around the main foil showed that an empirical estimation, assuming a symmetry plane between the two flaps underestimates the induced drag for the split-flaps, so a correction was derived from the CFD results. There is a very complex flow in the gap between the flaps and it depends on the flap loading. A reduced additional drag is observed when both flaps have a non-negative lift coefficient.

The AHSS performed well in the DVPP for the simulated gust scenarios, preventing capsize of the boat and reducing the speed loss during disturbances. Thereby reducing the effort of the sailors in stabilizing the boat and adding a performance increase during the race. With the decoupled system the heel stability of the boat is significantly increased during a gust without reducing the stable ride height.

Using the manual offset with a windward heel, a higher boat speed was achieved in the DVPP despite the additional induced drag with the split-flaps. The increased stability allowed the sails to be powered more compensating for the induced drag.

It should be mentioned, however, that the comparison depends on the modelling of the induced resistance. The correction of the effective aspect ratio is done with limited CFD simulations. Increasing the number of data points on the CFD studies will lead to a better empirical prediction of the induced drag of the split-flaps.

8. ACKNOWLEDGMENTS

The authors would like to acknowledge the help, expertise, and support provided by,

1. Chalmers Formula Sailing team of 2018 for designing and building Linnea.
2. Studies carried out by the Chalmers Formula Sailing team of 2019-20.
3. Chalmers University of Technology for providing software licenses and resources.

9. REFERENCES

Acerbi, T. et al. (2017). 'Chalmers Formula Sailing – High Performance Skiff'. Department of Mechanics and Maritime Sciences, Chalmers University of Technology.

Andersson, A. et al. (2018) 'Design of A Foiling Optimist', Journal of Sailboat Technology, pp. 1–24.

Bagué, A., Degroote, J., Demeester, T., & Lataire, E. (2021). 'Dynamic Stability Analysis of a Hydrofoiling Sailing Boat using CFD'. Journal of Sailing Technology, 6(1), 58–72.

Bacon, B. J., & Gregory, I. M. (2007). General equations of motion for a damaged asymmetric aircraft. AIAA Atmospheric Flight Mechanics Conference, 1, 63–75. https://doi.org/10.2514/6.2007-6306

Beaver, B. and Zseleczky, J. (2009) 'Full Scale Measurements on a Hydrofoil International Moth', Chesapeake Sailing Yacht Symposium. Annapolis, Maryland.

Boman, A. (2020) 'Design of a flight-control system for foiling dinghies with a T-wing and individual flaps'. BSc Thesis, Chalmers University of Technology.
url: https://hdl.handle.net/20.500.12380/301921

Caughy, D. A. (2011). 'Introduction to aircraft stability and control'. Sibley School of Mechanical & Aerospace Engineering, Cornell University

CAESES (2019), FRIENDSHIP SYSTEMS. url: https://www.caeses.com/

Drela, M. and Youngren, H. (2013) 'xfoil'. Available at: http://web.mit.edu/drela/Public/web/xfoil/

Eggert, F., Henrichs, J., Hansen, H., & Hochkirch, K. (2020). 'Flight Dynamics and Stability Assessment for an International Moth'. INNOVSAIL 2020.

Gerritsma, J., Onnink, R., & Versluis, A. (1981). 'Geometry, resistance and stability of the Delft systematic yacht hull series'. International Shipbuilding Progress, 28(328), 276–297. https://doi.org/10.3233/ISP-1981-2832801

Hansen, H., Hochkirch, K., Burns, I., & Ferguson, S. (2019). 'Maneuver Simulation and Optimization for AC50 Class'. Journal of Sailing Technology, 4(1), 142–160.

Heppel, P. (2015). 'Flight Dynamics of Sailing Foilers'. 5th High Performance Yacht Design Conference. Auckland,

Hoerner, S. F. (1957) 'Fluid Dynamic Drag'. Albuquerque, USA.

Hoerner, S. F., & Borst, H. V. (1975). 'Fluid-dynamic lift: Practical information on aerodynamic and hydrodynamic lift'. Brick Town, N.J: L.A. Hoerner.

Horel, B. (2019). 'System-based modelling of a foiling catamaran'. Ocean Engineering Journal, 171, 108–119.

Kerdraon, P., Horel, B., Bot, P., Letourneur, A., & Le Touzé, D. (2020). Development of a 6-DOF Dynamic Velocity Prediction Program for offshore racing yachts. Ocean Engineering Journal, 212, 107668. https://doi.org/10.1016/J.OCEANENG.2020.107668

Keller, T., Henrichs, J., Hochkirch, K., & Hochbaum, A C. (2017). 'Numerical Simulations of a Surface Piercing A-Class Catamaran Hydrofoil and Comparison against Model Tests'. Journal of Sailing Technology, Article 2017-04.

Larsson, L. Eliasson E, R & Orych, M. (2014). Principles of yacht design (4th ed.). International Marine : McGraw-Hill.

Larsson, L. Eliasson E, R & Orych, M. (2022). Principles of yacht design (5th ed.). London: Bloomsbury Publishing.

M. Faltinsen, O. (2005) 'Steady free-surface effects on a foil', in Hydrodynamics of High-Speed Marine Vehicles. Cambridge University Press, pp. 199–202.

Masuyama, Y. (1987). 'Stability analysis and prediction of performance for a hydrofoil sailing boat'. International Shipbuilding Progress, 34(390), 20–29. https://doi.org/10.3233/ISP-1987-3439001

MATLAB (2020), MathWorks, Inc. url: https://www.mathworks.com/products/matlab.html

Monsonnec, F. and Waller, N. (2015) The Foil Alphabet. Available at: http://proafile.com/multihull-boats/article/the-foil-alphabet

ORC VPP Documentation. (2019), Offshore Racing Congress. Available at: https://www.orc.org/rules/ORC%20VPP%20documentation%202019.pdf

Shampine, L. F., Gladwell, I., & Thompson, S. (2003). Solving ODEs with MATLAB. In Solving ODEs with MATLAB. Cambridge University Press. https://doi.org/10.1017/CBO9780511615542

Star CCM + (2018), Siemens Digital Industries Software.